



Orchestrated decline of Asian summer monsoon and Atlantic meridional overturning circulation in global warming period

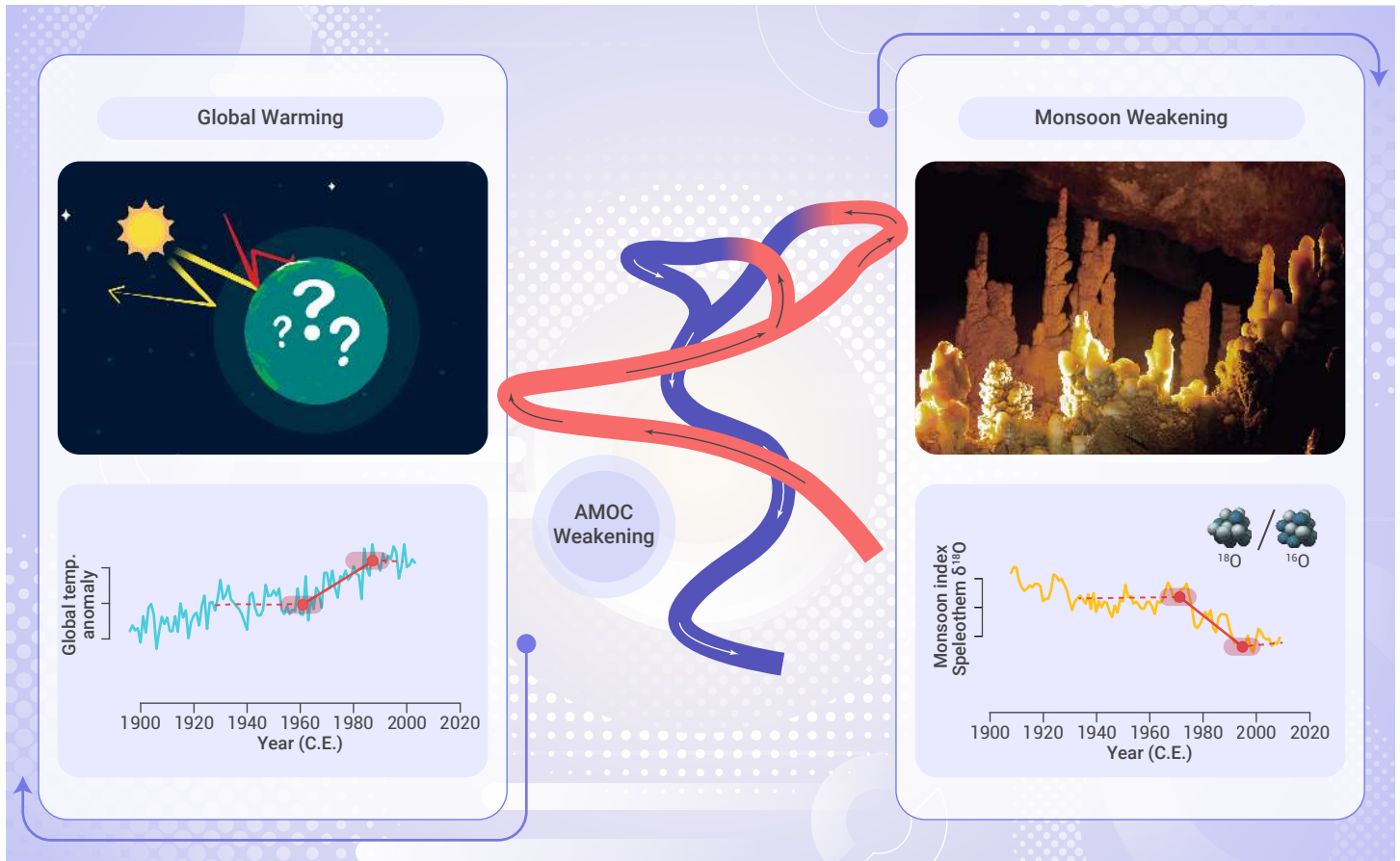
Jingyao Zhao,¹ Hai Cheng,^{1,2,*} Jie Cao,^{3,*} Ashish Sinha,^{1,4} Xiyu Dong,¹ Liangkang Pan,¹ Carlos Pérez-Mejías,¹ Haiwei Zhang,¹ Hanying Li,¹ Jian Wang,¹ Kexin Wang,¹ Jiahui Cui,¹ and Yan Yang⁵

*Correspondence: cheng021@xjtu.edu.cn (H.C.); caoj@ynu.edu.cn (J.C.)

Received: May 3, 2023; Accepted: May 26, 2023; Published Online: June 6, 2023; <https://doi.org/10.59717/j.xinn-geo.2023.100011>

© 2023 The Author(s). This is an open access article under the CC BY-NC-ND license (<http://creativecommons.org/licenses/by-nc-nd/4.0/>).

GRAPHICAL ABSTRACT



PUBLIC SUMMARY

- We present a high-quality speleothem $\delta^{18}O$ record from the Shandong Peninsula, covering the global warming period.
- The trend of the enriched speleothem $\delta^{18}O$ in global warming period mainly reflects dynamic facet of Asian summer monsoon.
- Decline of the Atlantic Meridional Overturning Circulation in global warming period may play a crucial role in the ASM weakening.



Orchestrated decline of Asian summer monsoon and Atlantic meridional overturning circulation in global warming period

Jingyao Zhao,¹ Hai Cheng,^{1,2,*} Jie Cao,^{3,*} Ashish Sinha,^{1,4} Xiyu Dong,¹ Liangkang Pan,¹ Carlos Pérez-Mejías,¹ Haiwei Zhang,¹ Hanying Li,¹ Jian Wang,¹ Xekin Wang,¹ Jiahui Cui,¹ and Yan Yang⁵

¹Institute of Global Environmental Change, Xi'an Jiaotong University, Xi'an 710054, China

²State Key Laboratory of Loess and Quaternary Geology, Institute of Earth Environment, Chinese Academy of Sciences, Xi'an 710061, China

³Department of Atmospheric Sciences, Yunnan University, Kunming 650500, China

⁴Department of Earth Science, California State University Dominguez Hills, Carson, CA 90747, USA

⁵Chongqing Key Laboratory of Karst Environment & School of Geographical Sciences, Southwest University, Chongqing 400715, China

*Correspondence: cheng021@xjtu.edu.cn (H.C.); caoj@ynu.edu.cn (J.C.)

Received: May 3, 2023; Accepted: May 26, 2023; Published Online: June 6, 2023; <https://doi.org/10.59717/j.xinn-geo.2023.100011>

© 2023 The Author(s). This is an open access article under the CC BY-NC-ND license (<http://creativecommons.org/licenses/by-nc-nd/4.0/>).

Citation: Zhao J., Cheng H., Cao J., et al., (2023). Orchestrated decline of Asian summer monsoon and Atlantic meridional overturning circulation in global warming period. *The Innovation Geoscience* 1(1).

The anthropogenic warming of the Earth's atmosphere is causing dynamical and thermodynamical changes in the ocean and atmosphere circulation, including the Asian summer monsoon (ASM) and the oxygen isotope compositions of its precipitation. Here we present a high-resolution speleothem $\delta^{18}\text{O}$ record from the Shandong Peninsula, eastern China with an age precision of ± 3 years, which in conjunction with five other existing high-resolution speleothem records from the ASM domain, reveals a robust weakening trend in the ASM during the global warming period, particularly since around the 1970s. During this period, both the decline of the Atlantic Meridional Overturning Circulation inferred from existing model-empirical records and the spatially heterogeneous pattern of global warming inferred from the coupled reanalysis of the 20th century (CERA-20C) product result in broadly similar changes in moisture flux pattern in the ASM domain. This, in turn, leads to the ASM weakening trend in terms of dynamics, as suggested by the speleothem $\delta^{18}\text{O}$ records.

INTRODUCTION

The Asian summer monsoon (ASM) is a dominant force in shaping the environment of a region where nearly half of the world's population resides.^{1,2} Understanding the dominant drivers of ASM variability is essential, especially in the context of ongoing global warming (GW).³ The greenhouse gas (GHG) forced warming of the Earth's atmosphere is theorized to have different impacts on ASM from the mix of dynamic and thermodynamic mechanisms.⁴⁻⁸ On one hand, the moisture content of the atmosphere is expected to increase due to enhanced water-holding capacity and higher vaporization latent heat which should lead to an increase in precipitable water and rainfall in the core ASM regions.⁹⁻¹⁰ Indeed, this is an important thermodynamic reason for increased rainfall under different GHG emissions scenarios in IPCC AR6. On the other hand, the GHG-induced changes in atmospheric circulation are expected to result in an overall increase in atmospheric stability, rather than the land-ocean atmosphere thermal/barometric contrast,¹¹⁻¹³ due to the roughly unchanged net energy input (NEI) over the land and ocean.

The projected ASM weakening of atmospheric circulation under the current GW^{7,8,15-18} is consistent with the southward shift of the intertropical convergence zone (ITCZ)⁸ and the slowdown of the Northern Hemisphere (NH) Hadley cell.^{7,19,20} Nonetheless, the response of ASM to GHG-induced global warming during the 20th century is not yet fully understood due to complicated physical processes such as ocean stratification and circulation,¹¹ inter-hemispheric temperature gradient under the current GW,⁸ and the role of increasing anthropogenic aerosols.²¹⁻²³

The Atlantic Meridional Overturning Circulation (AMOC) is one of the most important drivers of the ASM variability on sub-millennial to glacial-interglacial timescales²⁴⁻²⁵ as evidenced from both paleoclimate reconstructions^{1,2,25-27} and water hosing simulations.^{24,25,28-30} The AMOC typically has a strength of around 17 Sv (Sv = Sverdrup; 1 Sv = 10^6 m³/s) and is the largest source of northward oceanic heat transport. The redistribution of oceanic heat in the NH and Southern Hemisphere due to the AMOC has been shown to trigger bipolar anti-phased changes in temperature and monsoon rainfall during the last glacial period, such as those during the Dansgaard-Oeschger,

the Heinrich and Antarctic Isotope Maximum events.^{22,25} When the AMOC slows down or shuts down, it weakens the ASM by reducing the land-ocean temperature gradient, shifting the ITCZ southward, and weakening the Hadley cell in boreal summer by cooling the NH and transporting oceanic heat towards lower latitudes or the SH^{2,25,28,31} and *vice-versa*. Importantly, both the AMOC and ASM weakened in the 1970s concomitant with an acceleration in the global warming trend.⁸ The CMIP6 simulations project a decline of the AMOC in the future but it is still unclear how it will affect the ASM circulation. Therefore, it is essential to investigate the interactions between the AMOC and ASM on sub-millennial to multidecadal timescales to refine our understanding of their dynamics in a warming climate.

In recent decades, numerous research studies have attempted to characterize the link between ASM and GW.^{5,16-18} The speleothem $\delta^{18}\text{O}$ in ASM domains is one of the most important proxies that can unravel the past interactions between the ASM and AMOC.^{1,2,26,34-38} However, whether the GW and the weakening of AMOC influence the monsoon signal recorded by the speleothem $\delta^{18}\text{O}$ has not yet been thoroughly studied. To fully examine their relations and detect the physical mechanism on multidecadal timescale, we present a new high-resolution speleothem $\delta^{18}\text{O}$ record and integrate it with other existing records to characterize the ASM intensity during the last century.

GEOLOGICAL SETTING AND SAMPLE COLLECTION

Qujia cave (118.4° E, 35.7° N, 456 m a.s.l.) is located in southwest Yishui County, on the eastern margin of Mountain Meng, Shandong Province, eastern China (Figures 1 and S1). Mountain Meng (1156 m) is the second-highest mountain in Shandong Province, consisting mainly of ancient granites and metamorphic rocks, where limestones are scarce. The cave was formed in limestones of the Cambrian formation. It has an entrance of 3×4 m² and a length of >0.3 km. A calcite speleothem (QJ1) was collected ~100 m from the Qujia cave entrance in July 2017. The speleothem is 10.0 cm in height and 5.0 cm in diameter (Figure S2).

The ASM controls the hydroclimate with most of the rainfall (86%) in the area occurring during the wet season (May–October). The mean annual temperature and precipitation recorded in the Jvixian meteorological station (~5 km from the cave site) are 12.6°C and 793 mm (1960–2018 C.E.), respectively. The vegetation above the cave is secondary growth deciduous broadleaf trees and shrubs.

METHODS

²³⁰Th dating and Stable isotopes

Stalagmite QJ1 was split into two halves along the growth axis, and 11 powder subsamples (≤ 30 mg) were drilled from one of the polished slabs using a carbide dental burr of 0.3 mm diameter. The ²³⁰Th-dating analysis was performed at multi-collector inductively coupled plasma mass spectrometry (Neptune Plus, Thermo Scientific) in the Isotope Laboratory of Xi'an Jiaotong University. Chemical procedures for the separation and purification of uranium (U) and thorium (Th), as well as the methods of U and Th isotopic analysis, were described in Edwards et al. (1987), Cheng et al. (2000), Cheng et al. (2013) and Zhao et al. (2018). And all results are reported in Table 1. For stable isotope, powdered subsamples, each weighing 40–90 μg , were micro-

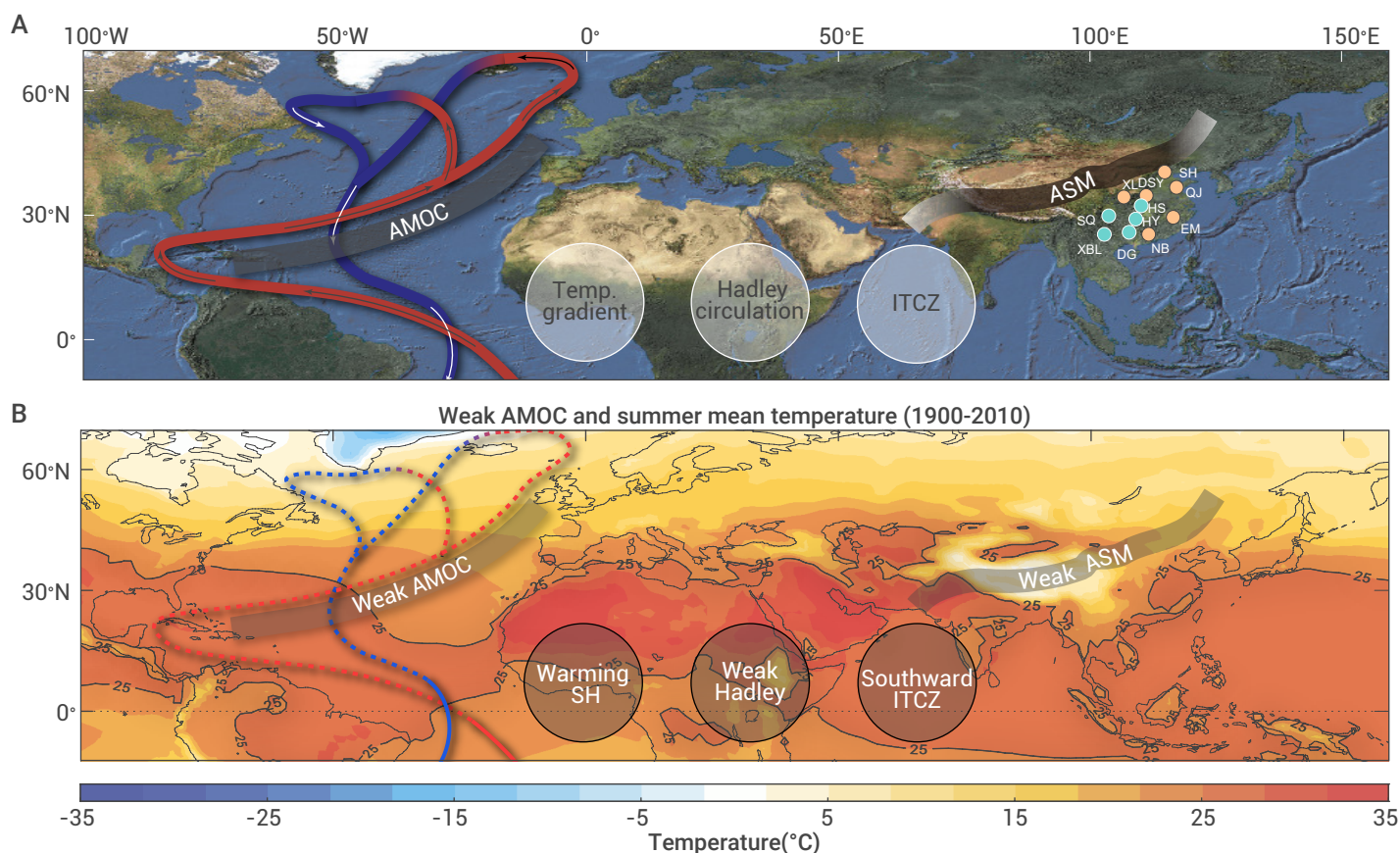


Figure 1. Conceptual diagram depicting the climatic connections between ASM and AMOC, and the location of caves are shown in the topographic map Qujia cave (QJ) (this study), Shihua cave (SH),³⁶ Dongshiyi cave (DSY),³⁴ Wuya cave (WY),⁴² Xianglong Cave (XL),⁵³ Heshang cave (HS),⁵⁶ Hongyan cave (HY),⁵⁶ E'mei cave (EM),³⁷ Shenqi cave (SQ),⁷⁷ Dongge cave (DG),⁵⁷ Xiaobailong cave (XBL)⁵¹ and Niubizi cave (NB).⁵⁴ The yellow circles point to high-resolution (higher than 1-year resolution) record sites. The summer (July-September) mean surface air temperature based on the CERA-20C gridded dataset,⁷⁸ and the Conceptual diagram depicting the climatic connections between weakening ASM and AMOC decline.

Table 1. ²³⁰Th dates of QJ1 speleothem. The error is 2σ error

Sample Number	Depth (mm)	²³⁸ U (ppb)	²³² Th (ppt)	²³⁰ Th / ²³² Th (atomic x10 ⁻⁶)	δ ²³⁴ U* (measured)	²³⁰ Th / ²³⁸ U (activity)	²³⁰ Th Age (yr) (uncorrected)	²³⁰ Th Age (yr) (corrected)	δ ²³⁴ U ^{initial**} (corrected)	²³⁰ Th Age (yr BP)*** (corrected)
QJ1-2	0.5	4758±16	3385±72	14±1	2101.2±7.4	0.0006±0.0000	22±2	15±5	2101±7	-52±5
QJ1-3	2.3	4295±4	1618±36	51±2	2134.9±2.1	0.0012±0.0000	41±2	37±3	2135±2	-30±3
QJ1-T	2.9	5616±461	1794±48	70±2	2123.8±23.3	0.0014±0.0001	47±4	44±4	2124±23	-23±4
QJ-D1	4.0	4625±20	600±15	259±17	2146.6±7.8	0.0020±0.0001	71±4	69±4	2147±8	1±4
QJ1-4	5.5	3200±3	244±18	477±37	2138.3±2.1	0.0022±0.0001	77±2	76±2	2139±2	9±2
QJ-D2	7.0	5240±23	232±10	1198±68	2166.1±7.2	0.0032±0.0001	111±4	111±4	2167±7	43±4
QJ-D3	8.5	5426±27	588±12	589±15	2165.6±8.3	0.0039±0.0001	133±2	132±2	2166±8	64±2
QJ1-5	11.5	6489±24	435±17	1138±46	2155.3±7.0	0.0046±0.0001	160±2	159±2	2156±7	92±2
QJ-D4	15.0	6958±30	566±21	1078±43	2156.6±7.8	0.0053±0.0001	184±3	183±3	2158±8	115±3
QJ1-6	19.0	7000±19	276±17	2348±142	2153.9±5.4	0.0056±0.0000	194±2	194±2	2155±5	127±2
QJ1-7	22.5	7146±16	108±16	7101±1046	2146.2±4.6	0.0065±0.0000	226±2	225±2	2148±5	158±2

U decay constants: $\lambda_{238} = 1.55125 \times 10^{-10}$ (Jaffey et al., 1971) and $\lambda_{234} = 2.82206 \times 10^{-6}$ (Cheng et al., 2013). * $\delta^{234}\text{U} = ([^{234}\text{U}/^{238}\text{U}]_{\text{activity}} - 1) \times 1000$. ** $\delta^{234}\text{U}_{\text{initial}}$ was calculated based on ²³⁰Th age (T), i.e., $\delta^{234}\text{U}_{\text{initial}} = \delta^{234}\text{U}_{\text{measured}} \times e^{\lambda_{234} \times T}$. Corrected ²³⁰Th ages assume the initial ²³⁰Th/²³²Th atomic ratio of $4.4 \pm 2.2 \times 10^{-6}$. Those are the values for a material at secular equilibrium, with the bulk earth ²³²Th/²³⁸U value of 3.8. The errors are arbitrarily assumed to be 50%. ***B.P. stands for "Before Present" where the "Present" is defined as the year 1950 C.E.

milled perpendicularly to the extension axes of QJ1 at 0.1 mm increments and analyzed in a Thermo Scientific MAT253 plus mass spectrometer

coupled with an online carbonate preparation device (Kiel IV) at the Isotope Laboratory, Xi'an Jiaotong University, China. Results are reported relative to

the Vienna Pee Dee Belemnite (VPDB) standard. The typical precision for $\delta^{18}\text{O}$ is 0.06‰ at the 1- σ (1σ). A total of ~400 isotope data were obtained, and the international standards TTB1 were added to the analysis for every 10 to 20 samples to check reproducibility.

Meteorology data and analysis methods

Assessments of trends and anomalies in the precipitation, temperature, and water-vapor fluxes in both spatial and temporal domain is key to the choice of gridded precipitation data. Recent studies evaluated several gridded datasets of meteorological data and concluded that CERA-20C³⁹ global datasets recently released by the ECMWF (European Centre for Medium-Range Weather Forecasts), well-replicate annual and seasonal mean and variability and probability distribution of observed temperature and water-vapor flux data from stations located within ASM region. The Experimental Climate Prediction Center's Isotope-incorporated Global Spectral Model (isoGSM) has been widely used for both modern and past climate simulations and was proved to be in good agreement with the $\delta^{18}\text{O}$ observations from Global Network of Isotopes in Precipitation (GNIP) stations globally.⁴⁰ The CERA-20C was used to analyze the spatial patterns of annual temperature anomalies and the spatial patterns of interannual rainfall variability.

In order to conduct a synthesis of six speleothem $\delta^{18}\text{O}$ records from the East Asian region, we used the Monte Carlo Empirical Orthogonal Function analysis (MCEOF) method, based on the following criteria: the proxy primarily reflects summer monsoon intensity; the proxy data was measured at a time interval of 1 year or less; the age model was based on highly precise ²³⁰Th-dating analysis; and the archive covers at least the last century (1908-2009 C.E.). The MCEOF method was applied to the data using 4,000 simulations, as described in ref 52. The code was implemented in MATLAB and involved iterative age modeling and eigendecomposition of the proxy time series to isolate common regional patterns and estimate uncertainties.

To identify objective change points in various records, we utilized two algorithms, namely the Ramp-fitting⁴¹ and Trend-fitting methods. The selection of the algorithm was based on the shape of the time-series. In the Ramp-fitting method, two change points (t_1 and t_2) were identified, and two constant levels of pre-transition ($t > t_2$) and post-transition ($t < t_1$) were estimated and fitted with a ramp between them. The data series underwent a Markov Chain Monte-Carlo (MCMC) sampler for $3e^6$ steps each. Global temperature records were calculated for the periods 1930-2009 C.E., while the entire period (1908-2009 C.E.) were used for PC1 and AMOC index. To further test the robustness of the identified change points, we employed another method wherein the "trends" were fitted to the entire time-series without prior setting of the search time window.

RESULTS

Chronology

Sample QJ1 has a high ²³⁸U concentration (3-7 ppm) and relatively low ²³²Th concentration (100-3000 ppt), which allows us to obtain high-precision ²³⁰Th dates with most dating errors less than 5 yrs (2σ) (Table 1). The stalagmite age model was constructed by OxCal Bayesian modeling software⁴² and Constructing Proxy Records from Age models (COPRA),⁴³ using the 11 ²³⁰Th dates ages (the average error: ± 3 years) obtained plus an additional assumption of age 2017 C.E. at the top of the stalagmite, since the growth was active at the time it was collected (Figure S2). Both modeling schemes yielded nearly identical results and the conclusions of this study are not sensitive to the choice of different age models (Figure S3). The QJ1 $\delta^{18}\text{O}$ record covers the last ~227 years (1787 to 2015 C.E.) with an average annual resolution (Figure S3). The $\delta^{18}\text{O}$ time series for QJ1 on an absolute time scale is obtained after 2000 Monte Carlo realizations of the age model by COPRA (Figure S2).

The $\delta^{18}\text{O}$ time series

In speleothem-based paleoclimate studies, it is crucial to test whether speleothem $\delta^{18}\text{O}$ reflects the $\delta^{18}\text{O}$ of meteoric precipitation and if the equilibrium fractionation was reached during speleothem calcite precipitation. Among various tests, the replication test is considered the most rigorous.⁴⁴ A broad resemblance ($r=0.71$, $p<0.01$) between our QJ1 $\delta^{18}\text{O}$ record and a previously published XMG-1 $\delta^{18}\text{O}$ record from Shihua cave, Beijing (Figure S3), suggests that the encoded signal mainly responds to overall

regional climate conditions, and hence the kinetic fractionation is minimal, suggesting conditions close to isotopic equilibrium during calcite precipitation. The $\delta^{18}\text{O}$ values range from -6.5 ‰ to -8.3 ‰ (average -7.6 ‰). While the QJ1 speleothem $\delta^{18}\text{O}$ record shows a trend towards more enriched values from around 1900 to 2017 C.E., with rather large age uncertainties, the rest segment reflects larger variations (Figures S2 and S3). The $\delta^{18}\text{O}$ record is characterized by a progressively increasing trend in the last century, which has been also documented in many other ASM speleothem $\delta^{18}\text{O}$ records.^{34,38,45}

DISCUSSION

Interpretation of the Chinese cave $\delta^{18}\text{O}$

The ASM is a vast climate system that dominates regional rainfall through large-scale circulation.^{1,25} The nature of ASM has been understood from two different perspectives: energetics and momentums.^{5,11,12} These perspectives characterize different parts of the ASM, but neither can fully describe the complexity of the system as in "blind men and giant elephant".²⁵ In the context of energetically directing circulation, the ASM exports moist static energy (MSE) away from the ascending branches and the concomitant precipitation. This perspective emphasizes the thermodynamic nature of the ASM, as it mainly describes the vertical transport of energy and moisture by the NEI. On the other hand, the momentum mainly characterizes the dynamic nature of the ASM's large-scale circulation.^{1,2,25} While local patterns in precipitation amount spatially elucidate an energetic difference in the ASM domains, the overall large-scale ASM circulation is generally characterized by the unified "gigantic land-sea breeze" (e.g., at 850 hPa or water vapor flux, Figures S4 and S5) primarily driven by the land-ocean barometric contrast at a vast spatial-scale.^{46,47} In other words, apart from the ASM's thermodynamic processes, ASM essentially has a dynamic nature that reflects the large-scale atmospheric circulations.

The ASM speleothem $\delta^{18}\text{O}$ records spanning the last century exhibit spatially consistent trends toward the enriched ¹⁸O values, suggesting a common climatic control (Figures 2 and 3), which explicitly stands in contrast to the regional divergent patterns of precipitation amount. Moreover, the seasonal variability of precipitation $\delta^{18}\text{O}$ also shows spatial consistency in the ASM domain, with enriched ¹⁸O values at the onset of the monsoon season and depleted ¹⁸O values during the main summer monsoon phase.^{35,48} In addition, tree-ring cellulose $\delta^{18}\text{O}$ records from the ASM regions, which are also influenced by precipitation $\delta^{18}\text{O}$ and relative humidity, can provide information about large-scale atmospheric circulation signals.^{49,50} Speleothem and tree-ring cellulose $\delta^{18}\text{O}$ records show significant positive correlations over the last century (Figure S6).

In short, the $\delta^{18}\text{O}$ values of speleothem archive are inversely correlated with summer monsoon dynamical intensity from seasonal to orbital timescales.^{1,26,35} High $\delta^{18}\text{O}$ values indicate decrease in moisture transport length linked to the weakening of southerly or summer monsoon circulation, while the low $\delta^{18}\text{O}$ values suggest increases in the distance of moisture sources related to the strengthening of southerly or summer monsoon circulation.^{25,34,35,51-54} Consequently, the regional consistent cave $\delta^{18}\text{O}$ signal mainly indicates the dynamic aspect of the monsoon circulation, with a small portion of the variability explained by local rainfall amount or thermodynamics.

ASM weakening under the current GW: speleothem $\delta^{18}\text{O}$ and observation

We conducted the conventional principal component (PCA) and Monte Carlo Empirical Orthogonal Function (MCEOF) analyses⁵ of multiple time series of high-resolution (≤ 1 year) and precisely dated (± 2 to ± 16 years errors with average ± 6.1 years) speleothem $\delta^{18}\text{O}$ data covering the 1908-2009 C.E. period to isolate common regional patterns and estimate uncertainties. The first principal component (PC1) and the EOF1 median demonstrated consistent patterns of variation (Figure 3). We considered the high-resolution and precisely dated speleothem records from Qujia (this study), Dongshiya,³⁴ E' mei,³⁷ Xianglong,⁵⁶ Shihua,³⁸ and Niubizi⁵⁷ caves (Figures 3, S7 and Table. S1). The PC1 explained 41% of the total variance. Moreover, we also used the MCEOF and PCA to analyze the set of speleothems $\delta^{18}\text{O}$ records with high-resolution (≤ 2 years) and precise age control (± 3 to ± 23 years errors with average ± 10.8 years), spanning the 1812-1983 C.E. period, including Qujia,

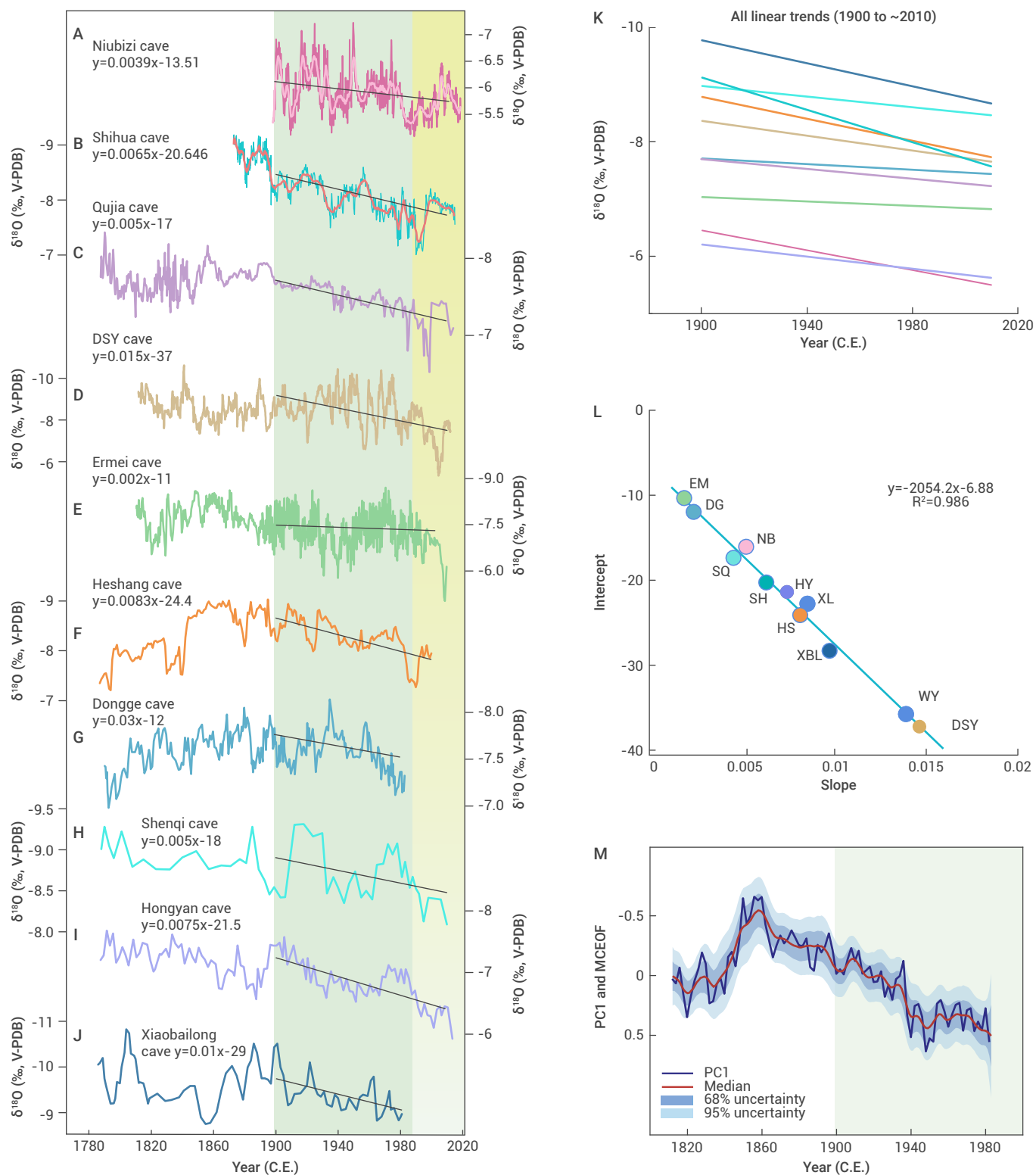


Figure 2. Comparison of the speleothem $\delta^{18}\text{O}$ records (same presented in Fig 1) from monsoonal China spanning the last ~200 years (A–J). The compilation of linear trends across the different speleothem $\delta^{18}\text{O}$ records (K and L). Results of the MCEOF and PCA analyses applied to timeseries of speleothem from Qujia (this study), Dongshiya,⁵⁴ E'mei,⁵⁷ Heshang,⁵⁵ Hongyan⁵⁶ and Dongge⁵⁷ caves (M). The gradually varied yellow bar shows the depleted- ^{18}O around the mid-1990s in speleothem $\delta^{18}\text{O}$ records (A–J). The green bars exhibit the linear fitting period (1900–2010 C.E.) (A–J and M). The EOF analysis shows median values (solid red line) and 68% and 95% two-tailed uncertainty bounds (blue shadings) empirically determined by 4000 simulations.

Dongshiya,⁵⁴ E'mei,⁵⁷ Heshang,⁵⁸ Hongyan⁵⁹ and Dongge⁶⁰ caves. The new results (Figure 2M) show the dominant trends similar to the previous results (Figure 3) in the contemporary interval (1908–1983 C.E.), indicating a common signal is extracted from 9 high-quality speleothem records. Both PC1 and EOF1 median suggest that the ASM circulation has significantly

weakened during the current GW period (Figure 3). It's consistent with the results from other speleothem $\delta^{18}\text{O}$ records from South Asia⁶¹ and Southeast Asia⁶² which also show a weakening trend in ASM circulation during this period.

Numerous observational studies have also shown that the ASM system

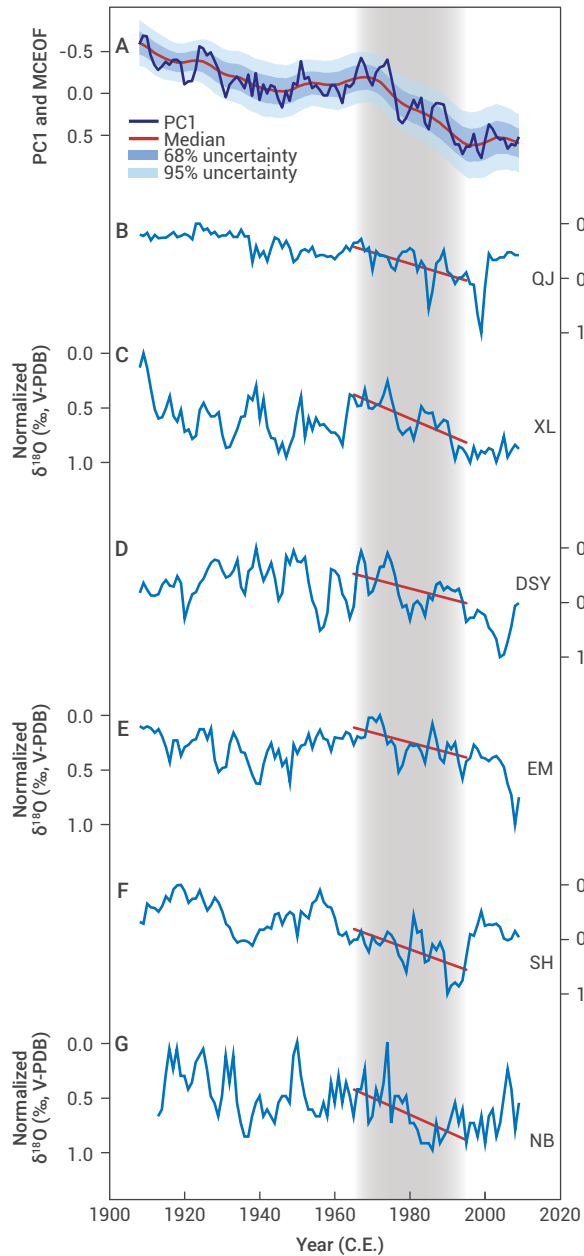


Figure 3. Results of the MCEOF and PCA analyses applied to timeseries of speleothem $\delta^{18}\text{O}$ records from China, including QJ1 (this study) The EOF analysis shows median values (navy blue line) and 68% and 95% two-tailed uncertainty bounds (blue shadings) empirically determined by 4000 simulations (A). The six speleothem $\delta^{18}\text{O}$ time series with annually interpolated resolution (light blue lines indicate data on their published age models). The speleothem $\delta^{18}\text{O}$ records correspond to Qujia cave (B) (this study), Xianglong Cave (C),⁵³ Dongshiya Cave (D),³⁴ E'mei Cave (E),³⁷ Shihua cave (F)³⁸ and Niubizi cave (G).⁵⁴ The red lines exhibit the linear trends in 1965-1995 C.E. periods (B-G).

has dynamically weakened due to the warming caused by GHG emissions.^{4,6,8,11,12} These results are supported by meteorological observations^{17,63} and model simulations.^{15,16} In addition, various Indian monsoon rainfall indices indicate a sustained drying trend during the last century (Figure S8), particularly after around the 1970s,^{22,61,63,64} while there are distinct divergent spatial patterns of precipitation from the EASM domain.^{34,46,53} The ASM circulation dynamical anomalies are primarily attributed to its net radiative forcing under the ongoing GHG-GW, which has led to increased atmospheric stability^{9,10,13} and changes in both the Hadley^{19,20} and Walker circulations.¹⁵ Additionally, there is a decline in the AMOC,^{31-33,65} The upper ocean stratification has also increased due to anthropogenic GHG forcing since 1970 C.E., as reported in IPCC AR6.

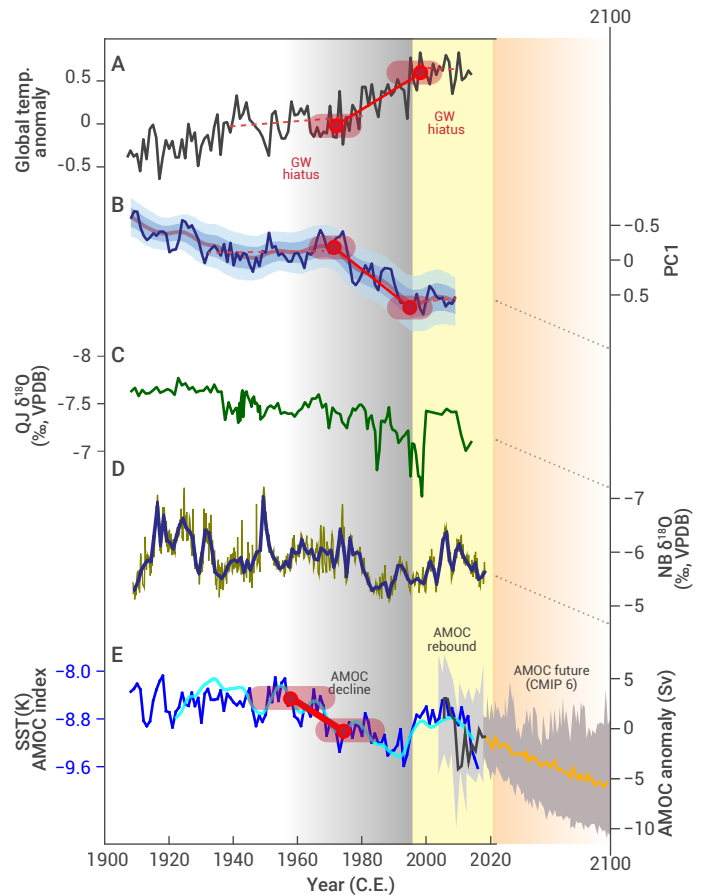


Figure 4. Comparison between the GW trend, speleothem records and AMOC variations over the past and future centuries (A) Global mean temperature anomaly (data from: <https://www.ncdc.noaa.gov/cag/global/time-series> in degrees Celsius). Red lines are the analysis results of Ramp-fitting⁶⁰ (solid) and Trend-fitting methods (dashed), while thick semi-red lines show the uncertainty of Ramp-fitting; (B) PC1 result of six speleothem records, as same as in Figure 3; Ramp-fitting analysis diagnosed the simultaneous alterations of both, that's in the global temperature increase and ASM weakening during the period of 1970-1995 C.E.; (C) the Qujia cave speleothem $\delta^{18}\text{O}$ record (this study); (D) Niubi cave speleothem $\delta^{18}\text{O}$ record. (E) AMOC index. In light blue is the AMOC anomaly as defined by HadCRUT4 data,⁶² in deep blue is the AMOC index defined via HadISST data;³² black curve shows the annual mean observed AMOC anomalies from RAPID;⁶² yellow curve illustrates the projected AMOC changes from CMIP5 simulation under SSP3-7 (IPCC report, 2022). 5-95% uncertainty range is shown with the vertical bars. The gray dotted lines indicate the possible transitional trends in the future. Note the inverted y-axis in (B-D). The different bars show the AMOC decline (gray), rebound (yellow) and simulated future (orange), respectively.

Indeed, there is a significant positive correlation ($r=0.8$, $p<0.01$) between ASM PC1 and global temperature variations, and also highly significant on annual to decadal timescales ($r=0.38$, $p<0.01$, linear detrended), as shown in Figures 4 and S7. The trend-fitting and Ramp-fitting analysis of PC1 reveals two periods of enriched ^{18}O (1908-1930 and 1966-1991 C.E.) and two periods of lightly depleted ^{18}O (1930-1966 and 1991-2009 C.E.) (Figure 4),⁶⁶ which are consistent with two periods of GW accelerations that occurred in the early and late twentieth century, as well as with two "GW hiatus" that took place during the mid-twentieth century and the early twenty-first century (Figures 4 and S7).^{66,67} Therefore, speleothem records further confirm that the ASM circulation has weakened and been very likely induced by the current GW.

ASM response to AMOC decline in a warming climate

The AMOC's influence on ASM intensity has been previously noted across the transitions between Greenland's warm interstadial and cool stadial during both glacial and interglacial periods.^{2,32,35} The AMOC decline leads to a reduction of energy transport from the ocean towards the NH, resulting in the cooling of the subpolar latitudes.³² During the past century, the AMOC strength declined in the 1970s followed by a rebound around the mid-1990s as

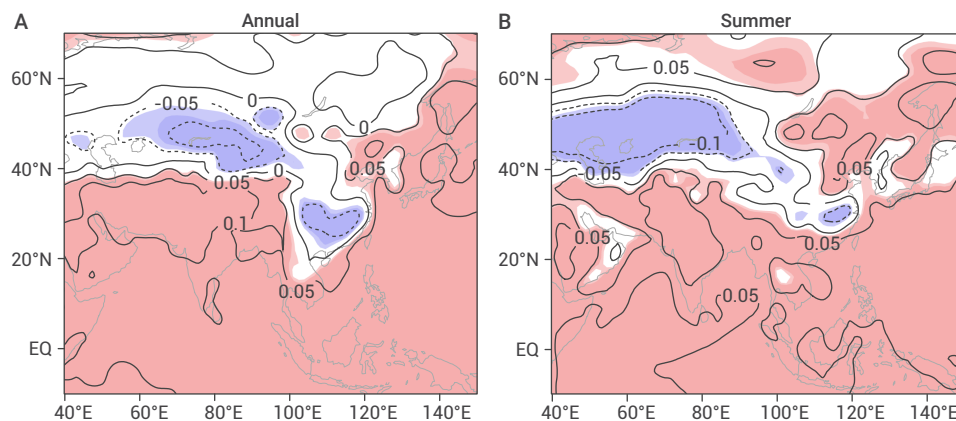


Figure 5. Linear trends ($^{\circ}\text{C decade}^{-1}$) in the ASM domains from 1901 to 2010 during the annual (A) and summer months (JJAS)(B) Univariate regression analyses are based on the CERA-20C grided dataset.⁷⁶ The increasing (decreasing) areas passing the significance test at the 95% and 99% confidence levels are shown by shaded areas with light red (blue) and red (blue), respectively.

evidenced in the model and SST reanalysis datasets (Figure 4E).^{28,31,32,65} This pattern of AMOC variability is broadly similar to the ASM variations observed in the speleothem $\delta^{18}\text{O}$ records, such as from Shihua, Niubizi, and Qujia caves as well as the PC1 (Figures 2 and 4). While the ASM rebound in PC1 is unclear possibly due to the limited available growth time until 2009, the ASM weakening was clearly punctuated in the mid-1990s, as diagnosed by the Ramp-fitting analysis (Figure 4B). To examine this further, we investigate the links between the moisture flux pattern in the ASM circulation and the AMOC decline in the context of the current GW, as discussed below.

AMOC decline and its impact under the current GW. Since the mid-twentieth century, the AMOC has declined by approximately 3 ± 1 Sv, which translates to roughly a 15% decrease.^{31,33,65} This decline is particularly prominent since around the 1970s (Figure 4E) and is characterized by a distinct spatial and SST “fingerprint” that displays cooling in the subpolar North Atlantic Ocean and warming in the Gulf Stream region.^{31–33} The pattern is seen in a range of model simulations from the CMIP5 project and is attributed to a slowdown in the AMOC coupled with reduced northward heat transport as well as a northward shift of the Gulf Stream.³³ Despite the highly nonlinear nature of the AMOC system and its response to GHG-GW,^{8,32} the majority of current GHG-forcing models predict a future decline in the AMOC in the CMIP6 project.^{8,31}

The AMOC decline can significantly affect the spatial heterogeneity pattern of GW, weakening the poleward heat transport and creating a weak north-south meridional thermal gradient by cooling the NH and warming the SH.^{8,24} Indeed, the spatial pattern of summer global warming is not uniform (Supplementary Text 2). One maximum warming area in summer is located mainly in the northern part of continental Asia, near the northern mid-high latitudes (Figure 5B). The forcing of the GHG “Arctic amplification” mechanism could be responsible for the consistent warming in this area.^{70–72} The other area of maximum warming is located near the tropical Indian Ocean, within the southwest margins of the ASM, while the middle part of the ASM domain exhibits a cooling trend over the last century (Figure 5B).^{73,74} Some studies have attributed the GW aspatial heterogeneity over ASM domains to the integrated effects of GHG and the relevant AMOC, as the simulation results.⁸ Additionally, the “sandwich pattern” of temperature has been shown to play a significant role in the formation of anomalous moisture flux patterns over the ASM domains (Figures 5 and 6). This often leads to the anomalous anticyclonic moisture fluxes, as described in the section below. In addition, there is evidence to suggest that the weakened large-scale boreal summer mean Hadley cell and a southward shift of the ITCZ under the current GW⁷⁵ and relevant AMOC decline forcing⁸ can weaken cross-equatorial airflows and corresponding southwest moistures.^{8,20}

Anomalous moistures flux pattern in ASM domain under the current GW. The spatial analysis of the climatological vertical NCAR water vapor flux in 1980–2010 C.E. reveals that during the summer monsoon season, water vapor is transported from the Bay of Bengal and western Pacific–South China Sea to the ASM regions primarily through southwesterly and southerly winds (Figure S5).^{34,45,76} Column-integrated moisture fluxes were regressed onto the QJ1 $\delta^{18}\text{O}$ record and the PC1 of the speleothem records (1908–2009 C.E.). The results show anomalous moisture flux with anticyclonic patterns

northerly anomalies to their east and significant easterly anomalies to their south, consistent with the previous studies.^{6,8} Another anticyclonic anomaly arises over the western North Pacific with significant easterly anomalies (Figure 6). Consequently, with the synthesized results of the anomalous moisture patterns over the ASM domain, southwest oceanic moisture in the ASM domain appears to have decreased (Figure 6). Interestingly, during the short “GW hiatus” (1945–1975 C.E.),^{67,68} the opposite pattern of anomalous moisture fluxes emerged over the ASM domain (Figure S9), indicating the relatively stable intensity of the ASM.

These findings suggest a potential physical mechanism underlying the significant connection between ASM circulation, GW and AMOC. Specifically, the weakening trend of the ASM inferred from speleothem $\delta^{18}\text{O}$ records may be attributed to the anomalous moisture flux patterns caused by the “temperature sandwich pattern” associated with the current GW (Figures 5 and S10). Several physical processes have been proposed as potential causes of it, including the AMOC decline,⁸ anthropogenic aerosols increasing,⁷⁷ SST changes in oceanic basins,⁵⁴ and Arctic amplification,⁷⁸ etc. However, none of them are conclusive up till now. We find the significant relation between the AMOC index and PC1 ($r=0.44$, $p<0.01$), as well as global temperature variations ($r=-0.56$, $p<0.01$) (Figures 4 and S11). They lead to the southward retreat of moisture, reducing moisture transported from upstream areas, and even southward shifts of major hydroclimatic elements such as the tropical monsoon trough, the subtropical Meiyu-Baiu-Changma front in East Asia, the western Pacific subtropical high and westerly jets (Figure S12).^{18,64,75,76}

While the exact changes in the AMOC during the 20th century are still a topic of ongoing research, multiple studies have suggested that the AMOC has weakened with the GW.^{31–33,65} The IPCC AR6 report also highlights the high likelihood of further decline of AMOC throughout the 21st century which is irreversible over the course of the next few centuries. Since the weakening ASM is strongly related to AMOC declines both under the current GW and in other geological periods,^{1,2,8,24,25,29} this gives rise to the concern that dynamically weakened ASM may further intensify rainfall and flooding in southern China in the near-term future as it did during the Little Ice Age.^{51,79,80}

CONCLUSIONS

Our new high-resolution (~ 1 year) and precisely dated (± 3 years error) speleothem $\delta^{18}\text{O}$ record from Shandong Province further confirms the long-term weakening trend of the ASM in the last century. The PC1 and MCEOF of the six high-resolution speleothem $\delta^{18}\text{O}$ records from China are correlated to the global temperature variability, showing two periods of slowdown and two periods of acceleration that mimics the GW signal seen in the last century. Diagnostic results using the CERA-20C dataset indicate that the GW spatial heterogeneity, likely induced by the GHG and the relevant AMOC, has led to a decrease in the meridional temperature gradient and an increase in anticyclone anomaly over the East Asian continent, thus dynamically weakening the ASM in the last century. This observation also underpins that the coherent speleothem $\delta^{18}\text{O}$ changes in the ASM region are a manifestation of large-scale changes in the summer monsoon circulation in tropics-subtropics. Our analyses provide new insights into the conditions that have led to the

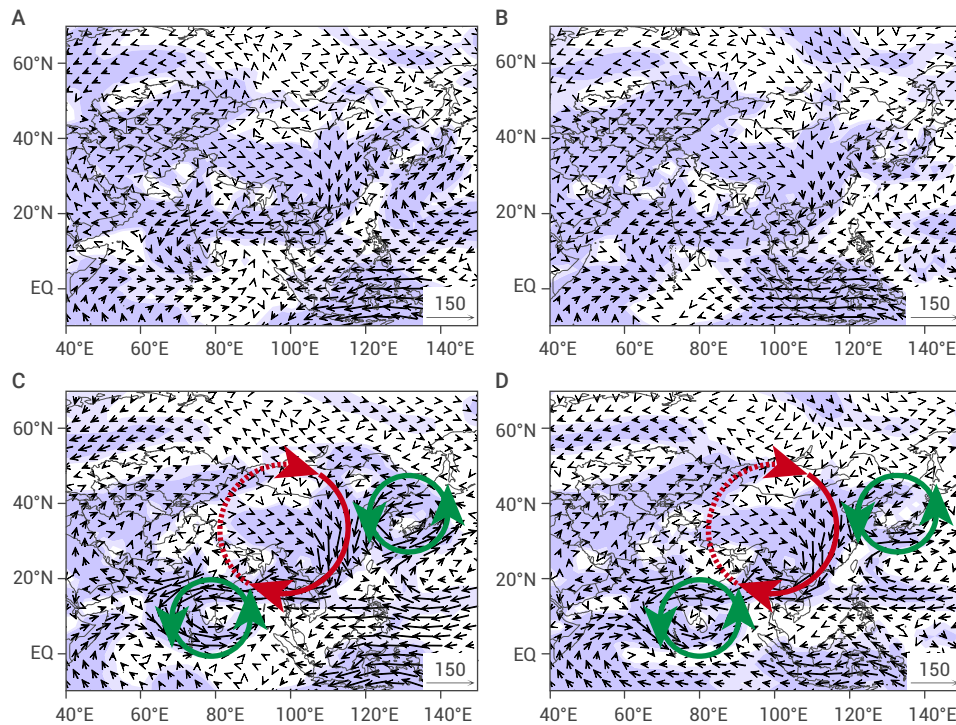


Figure 6. Anomalous column-integrated water-vapor fluxes regressed with the QJ1 $\delta^{18}\text{O}$ records (A, C) and PC1 (B, D) Water-vapor fluxes (unit: $\text{kg m}^{-1} \text{s}^{-1}$) integrate from 1000 to 100 hPa during the entire year (A, B) and during the rainy season (June–September) (C, D) during 1908–2009. Water-vapor fluxes are based on the monthly reanalysis data from the CERA-20C data recently released by the ECMWF (European Centre for Medium-Range Weather Forecasts). The resolution used is 2.5° latitude \times 2.5° longitude and 27 pressure levels from 1000 to 100 hPa. The areas passing the significance test at the 95% and 99% confidence levels are shown by shaded areas with light purple and dark purple, respectively. The red and green circles (C and D) respectively indicate the anticyclone and cyclone.

monsoon dynamically weakening under the current GW, and the role that AMOC plays in modulating these speleothem $\delta^{18}\text{O}$ variations regardless of varying warming or cooling conditions.

REFERENCES

- Cheng, H., Zhang, H.W., Cai, Y.J., et al. (2021). Orbital-scale Asian summer monsoon variations: Paradox and exploration. *Sci. China-Earth Sci.* **64**: 529–544. DOI: 10.1007/s11430-020-9720-y.
- Cheng, H., Xu, Y., Dong, X.Y., et al. (2021). Onset and termination of Heinrich Stadial 4 and the underlying climate dynamics. *Commun. Earth Environ.* **2**, 230.
- Cheng, H. (2020). Future Earth and Sustainable Developments. *The Innovation* **1**: 100055.
- D'Agostino, R., Bader, J., Bordoni, S., et al. (2019). Northern Hemisphere Monsoon Response to Mid - Holocene Orbital Forcing and Greenhouse Gas - Induced Global Warming. *Geophys. Res. Lett.* **46**: 1591-1601.
- Biasutti, M., Voigt, A., Boos, W.R., et al. (2018). Global energetics and local physics as drivers of past, present and future monsoons. *Nat. Geosci.* **11**: 392–400. DOI: 10.1038/s41561-018-0137-1.
- Li, Z.B., Sun, Y., Li, T., et al. (2021). Projections of South Asian Summer Monsoon Under Global Warming from 1.5° to 5°C . *J. Clim.* **34**: 7913–7926.
- Kossin, J. P. A global slowdown of tropical-cyclone translation speed. *Nature* **558**, 104–107.
- Sandeep, N., Swapna, P., Krishnan, R., et al. (2020). South Asian monsoon response to weakening of Atlantic meridional overturning circulation in a warming climate. *Clim. Dyn.* **54**: 3507–3524.
- Held, I. M. and Soden, B. J. (2006). Robust responses of the hydrological cycle to global warming. *J. Clim.* **19**: 5686–5699. DOI: 10.1175/JCLI3990.1.
- Trenberth, K. E. (1998). Atmospheric Moisture Residence Times and Cycling: Implications for Rainfall Rates and Climate Change. *Clim. Change* **39**: 667–694. DOI: 10.1023/A:1005319109110.
- Cheng, J., Ma, W.Y., Liu, Z.Y., et al. (2019). Varying Sensitivity of East Asia Summer Monsoon Circulation to Temperature Change Since Last Glacial Maximum. *Geophys. Res. Lett.* **46**: 9103–9109. DOI: 10.1029/2019GL083405.
- Jalihal, C., Srinivasan, J. and Chakraborty, A. (2020). Different precipitation response over land and ocean to orbital and greenhouse gas forcing. *Sci. Rep.* **10**: 11891. DOI: 10.1038/s41598-020-68346-y.
- Knutson, T. R. and Manabe, S. (1995). Time-mean response over the tropical Pacific to increased CO_2 in a coupled ocean-atmosphere model. *J. Clim.* **8**: 2181–2199. DOI: 10.1175/1520-0442(1995)008<2181:TMROTT>2.0.CO;2.
- Kitoh, A., Endo, H., Kumar, K.K., et al. (2013). Monsoons in a changing world: A regional perspective in a global context. *J. Geophys. Res.-Atmos.* **118**: 3053–3065. DOI: 10.1002/jgrd.50258.
- Vecchi, G. A., Soden, B.J., Wittenberg, A.T., et al. (2006). Weakening of tropical Pacific atmospheric circulation due to anthropogenic forcing. *Nature* **441**, 73–76.
- Endo, H., Kitoh, A., and Ueda, H. (2018). A Unique Feature of the Asian Summer Monsoon Response to Global Warming: The Role of Different Land–Sea Thermal Contrast Change between the Lower and Upper Troposphere. *Sola*. **14**: 57–63. DOI: 10.2151/sola.2018-010.

s41586-023-05903-1.

- Xie, X., Myhre, G., Liu, X.D., et al. (2020). Distinct responses of Asian summer monsoon to black carbon aerosols and greenhouse gases. *Atmos. Chem. Phys.* **20**: 11823–11839. DOI: 10.5194/acp-20-11823-2020.
- Bollasina, M. A., Ming, Y., and Ramaswamy, V. (2011). Anthropogenic aerosols and the weakening of the South Asian summer monsoon. *Science* **334**: 502–505. DOI: 10.1126/science.1204994.
- Liu, Y., Cai, W.J., Sun, C.F., et al. (2019). Anthropogenic Aerosols Cause Recent Pronounced Weakening of Asian Summer Monsoon Relative to Last Four Centuries. *Geophys. Res. Lett.* **46**: 5469–5479. DOI: 10.1029/2019GL082497.
- Zhang, R., and Delworth, T. L. (2005). Simulated Tropical Response to a Substantial Weakening of the Atlantic Thermohaline Circulation. *J. Clim.* **18**: 1853–1860. DOI: 10.1175/JCLI3460.1.
- Cheng, H., Li, H.Y., Sha, L.J., et al. (2022). Milankovitch theory and Innovation **3**: 100338.
- Wang, Y.J., Cheng, H., Edwards R.L., et al. (2001). A high-resolution absolute-dated late Pleistocene Monsoon record from Hulu Cave, China. *Science* **294**: 2345–2348. DOI: 10.1126/science.1064618.
- Cheng, H., Edwards R.L., Wang, Y.J., et al. (2006). A penultimate glacial monsoon record from Hulu Cave and two-phase glacial terminations. *Geology* **34**: 217–220.
- Bellomo, K., Meccia, V.L., D'Agostino, R., et al. (2023). Impacts of a weakened AMOC on precipitation over the Euro-Atlantic region in the EC-Earth3 climate model. *Clim. Dyn.*
- Woollings, T., Gregory, J. M., Pinto, J. G., et al. (2012). Response of the North Atlantic storm track to climate change shaped by ocean–atmosphere coupling. *Nat. Geosci.* **5**: 313–317. DOI: 10.1038/ngeo1438.
- Liu, W., Xie, S.-P., Liu, Z.Y., and Zhu, J. (2017). Overlooked possibility of a collapsed Atlantic Meridional Overturning Circulation in warming climate. *Sci. Adv.* **3**: e1601666. DOI: 10.1126/sciadv.1601666.
- Jackson, L.C., Biastoch, A., Buckley, M.W., et al. (2023). The evolution of the North Atlantic AMOC since 1980. *Nat. Rev. Earth Environ.* **3**: 241–254.
- Caesar, L., Rahmstorf, S., Robinson, A., et al. (2018). Observed fingerprint of a weakening Atlantic Ocean overturning circulation. *Nature* **556**: 191–196. DOI: 10.1038/s41586-018-0006-5.
- Marcello, F., Tonelli, M., Ferrero, B., and Wainer, I. (2023). Projected Atlantic overturning slow-down is to be compensated by a strengthened South Atlantic subtropical gyre. *Commun. Earth Environ.* **4**: 92. DOI: 10.1038/s43247-023-00750-4.
- Zhao, J.Y., Cheng, H., Yang, Y., et al. (2018). Reconstructing the western boundary variability of the Western Pacific Subtropical High over the past 200 years via Chinese cave oxygen isotope records. *Clim. Dyn.* **56**: 3741–3757.
- Cheng, H., Sinha, A., Wang, X.F., Cruz, F.W., et al. (2012). The Global Paleomonsoon as seen through speleothem records from Asia and the Americas. *Clim. Dyn.* **39**: 1045–1062. DOI: 10.1007/s00382-012-1363-7.
- Cheng, H., Zhang, H.W., Spötl, C., et al. (2020). Timing and structure of the Younger Dryas event and its underlying climate dynamics. *Proc. Natl. Acad. Sci. U. S. A.* **117**: 23408–23417. DOI: 10.1073/pnas.2007869117.
- Zhang, H., Cheng, H., Spötl, C., et al. (2018). A 200-year annually laminated stalagmite record of precipitation seasonality in southeastern China and its linkages to ENSO and PDO. *Sci. Rep.* **8**: 12344. DOI: 10.1038/s41598-018-30112-6.
- Li, X.L., Cheng, H., Tan, L.C., et al. (2017). The East Asian summer monsoon variability

- over the last 145 years inferred from the Shihua Cave record, North China. *Sci. Rep.* **7**: 7078. DOI: 10.1038/s41598-017-07251-3.
39. Laloyaux, P., Boisseson, E.D., Balmaseda, M., et al. (2018). CERA - 20C: A coupled reanalysis of the twentieth century. *J. Adv. Model. Earth Syst.* **10**: 1172–1195. DOI: 10.1029/2018MS001273.
 40. Yoshimura, K., Kanamitsu, M., Noone, D., and Oki, T. (2008). Historical isotope simulation using Reanalysis atmospheric data. *J. Geophys. Res.* **113**
 41. Capron, E., Rasmussen, S.O., Popp, T.J., et al. (2021). The anatomy of past abrupt warmings recorded in Greenland ice. *Nat. Commun.* **12**: 2106. DOI: 10.1038/s41467-021-22241-w.
 42. Ramsey, C. B. (2008). Deposition models for chronological records. *Quat. Sci. Rev.* **27**: 42–60. DOI: 10.1016/j.quascirev.2007.01.019.
 43. Breitenbach, S. F. M., Rehfeld, K., Goswami, B., et al. (2012). CO₂ Constructing Proxy Records from Age models (COPRA). *Clim. Past.* **8**: 1765–1779. DOI: 10.5194/cp-8-1765-2012.
 44. Dorale, J. A. and Liu, Z. (2009). Limitations of Hendsy test criteria in judging the paleoclimatic suitability of speleothems and the need for replication. *J. Cave Karst Stud.* **71**: 73–80.
 45. Tan, L.C., An, Z.S., Hub, C.-A., et al. (2014). Cyclic precipitation variation on the western Loess Plateau of China during the past four centuries. *Sci. Rep.* **4**: 6381. DOI: 10.1038/srep06381.
 46. Ding, Y.H., Wang, Z.Y., and Sun, Y. (2008). Inter - decadal variation of the summer precipitation in East China and its association with decreasing Asian summer monsoon. Part I: Observed evidences. *Int. J. Climatol.* **28**: 1139–1161.
 47. Wang, B., Wu, Z.W., Li, J.P., et al. (2008). How to Measure the Strength of the East Asian Summer Monsoon. *J. Clim.* **21**: 4449–4463. DOI: 10.1175/2008JCLI2183.1.
 48. Zhao, J.Y., Tan, L.C., Li, D., et al. (2022). The Seasonally Altered Atmosphere Moisture Circulations With Rainfall and Rainfall Isotopes in Southwest China. *Front. Earth Sci.* **10**: 795857. DOI: 10.3389/feart.2022.795857.
 49. Roden, J.S., Lin, G.H., and Ehleringer, J.R. (2000). A mechanistic model for interpretation of hydrogen and oxygen isotope ratios in tree-ring cellulose. *Geochim. Cosmochim. Acta* **64**: 21–35. DOI: 10.1016/S0016-7037(99)00195-7.
 50. Xu, C.X., Zhao, Q.Y., An, W.L., et al. (2021). Tree-ring oxygen isotope across monsoon Asia: Common signal and local influence. *Quat. Sci. Rev.* **269**: 107156. DOI: 10.1016/j.quascirev.2021.107156.
 51. Zhao, J.Y., Cheng, H., Yang, Y., et al. (2021). Role of the Summer Monsoon Variability in the Collapse of the Ming Dynasty: Evidences From Speleothem Records. *Geophys. Res. Lett.* **48**: 93071.
 52. Duan, W.H., Ruan, J.Y., Luo, W.J., et al. (2016). The transfer of seasonal isotopic variability between precipitation and drip water at eight caves in the monsoon regions of China. *Geochim. Cosmochim. Acta* **183**: 250–266. DOI: 10.1016/j.gca.2016.03.037.
 53. Tan, M. (2014). Circulation effect: response of precipitation δ 18 O to the ENSO cycle in monsoon regions of China. *Clim. Dyn.* **42**: 1067–1077. DOI: 10.1007/s00382-013-1732-x.
 54. Cheng, H., Zhang, H.W., Zhao, J.Y., et al. (2019). Chinese stalagmite paleoclimate researches: A review and perspective. *Sci. China Earth Sci.* **62**: 1489–1513. DOI: 10.1007/s11430-019-9478-3.
 55. Anchukaitis, K.J., and Tierney, J.E. (2012). Identifying coherent spatiotemporal modes in time-uncertain proxy paleoclimate records. *Clim. Dyn.* **41**: 1291–1306.
 56. Tan, L.C., Cai, Y.J., Cheng, H., et al. (2015). Climate significance of speleothem δ 18O from central China on decadal timescale. *J. Asian Earth Sci.* **106**: 150–155. DOI: 10.1016/j.jseaes.2015.03.008.
 57. Lu, J.Y., Zhang, H.W., Li, H.Y., et al. (2021) A 120-year seasonally resolved speleothem record of precipitation seasonality from southeastern China. *Quat. Sci. Rev.* **264**, 107023.
 58. Wang, M.Y., Hu, C.Y., Liu, Y.H., et al. (2022). Precipitation in eastern China over the past millennium varied with large-scale climate patterns. *Commun. Earth Environ.* **3**: 321. DOI: 10.1038/s43247-022-00664-7.
 59. Duan, F.C., Zhang, Z.Q., Liu, D.B., et al. (2022). A new stalagmite oxygen isotope record over the last 1350 years: Insights into spatial variation in Asian summer monsoon and temperature forcing. *Quat. Sci. Rev.* **284**: 107499. DOI: 10.1016/j.quascirev.2022.107499.
 60. Zhao, K. Wang, Y.J., Edwards, R. L., et al. (2015). A high-resolved record of the Asian Summer Monsoon from Dongge Cave, China for the past 1200 years. *Quat. Sci. Rev.* **122**: 250–257.
 61. Sinha, A. Kathayat, G., Cheng, H., et al. (2015). Trends and oscillations in the Indian summer monsoon rainfall over the last two millennia. *Nat. Commun.* **6**: 6309. DOI: 10.1038/ncomms7309.
 62. Tan, L.C., Shen, C.-C., Löwemark, L., et al. (2019). Rainfall variations in central Indo-Pacific over the past 2,700 y. *Proc. Natl. Acad. Sci. U. S. A.* **116**: 17201–17206. DOI: 10.1073/pnas.1903167116.
 63. Roxy, M.K., Ritika, K., Terray, P., et al. (2015). Drying of Indian subcontinent by rapid Indian Ocean warming and a weakening land-sea thermal gradient. *Nat. Commun.* **6**: 7423. DOI: 10.1038/ncomms8423.
 64. Huang, X. Zhou, T.J., Turner, A., et al. (2020). The Recent Decline and Recovery of Indian Summer Monsoon Rainfall: Relative Roles of External Forcing and Internal Variability. *J. Clim.* **33**: 5035–5060. DOI: 10.1175/JCLI-D-19-0833.1.
 65. Rahmstorf, S. Box, J.E., Feulner, G., et al. (2015). Exceptional twentieth-century slowdown in Atlantic Ocean overturning circulation. *Nat. Clim. Chang.* **5**: 475–480. DOI: 10.1038/nclimate2554.
 66. Kosaka, Y. and Xie, S.-P. (2016). The tropical Pacific as a key pacemaker of the variable rates of global warming. *Nat. Geosci.* **9**: 669–673. DOI: 10.1038/ngeo2770.
 67. Yao, S.-L., Luo, J.-J., Huang, G., and Wang, P.F. (2017). Distinct global warming rates tied to multiple ocean surface temperature changes. *Nat. Clim. Chang.* **7**: 486–491. DOI: 10.1038/nclimate3304.
 68. Gregory, J.M., Bouttes N., Griffies, S.M., et al. (2016). The Flux-Anomaly-Forced Model Intercomparison Project (FAFMIP) contribution to CMIP6: investigation of sea-level and ocean climate change in response to CO₂ forcing. *Geosci. Model Dev.* **9**: 3993–4017. DOI: 10.5194/gmd-9-3993-2016.
 69. Lenton, T.M., Held, H., Kriegler, E., et al. (2008). Tipping elements in the Earth's climate system. *Proc. Natl. Acad. Sci. U. S. A.* **105**: 1786–1793. DOI: 10.1073/pnas.0705414105.
 70. You, Q.L., Cai, Z.Y., Pepin, N., et al. (2021). Warming amplification over the Arctic Pole and Third Pole: Trends, mechanisms and consequences. *Earth-Sci. Rev.* **217**: 103625. DOI: 10.1016/j.earscirev.2021.103625.
 71. Coumou, D., Di Capua, G., Vavrus, S., et al. (2018). The influence of Arctic amplification on mid-latitude summer circulation. *Nat. Commun.* **9**: 2959. DOI: 10.1038/s41467-018-05256-8.
 72. Cohen, J., Screen, J.A., Furtado, J.C., et al. (2014). Recent Arctic amplification and extreme mid-latitude weather. *Nat. Geosci.* **7**: 627–637. DOI: 10.1038/ngeo2234.
 73. Wu, G.X., Li, Z.Q., Fu, C.B., et al. (2015). Advances in studying interactions between aerosols and monsoon in China. *Sci. China-Earth Sci.* **59**: 1–16.
 74. Zhang, L., and Li, T. (2016). Relative roles of anthropogenic aerosols and greenhouse gases in land and oceanic monsoon changes during past 156 years in CMIP5 models. *Geophys. Res. Lett.* **43**: 5295–5301. DOI: 10.1002/2016GL069282.
 75. Sun, Y., Ding, Y.H., and Dai, A.G. (2010). Changing links between South Asian summer monsoon circulation and tropospheric land-sea thermal contrasts under a warming scenario. *Geophys. Res. Lett.* **37**.
 76. Yang, Y., Yang, R.W., Cao, J., et al. (2019). Relationship between the Asian summer monsoon circulation and speleothem δ 18O of Xiaobailong cave. *Clim. Dyn.* **53**: 6351–6362. DOI: 10.1007/s00382-019-04935-6.
 77. Dong, B.W., Wilcox, L.J., Highwood, E.J., and Sutton, R.T. (2019). Impacts of recent decadal changes in Asian aerosols on the East Asian summer monsoon: roles of aerosol–radiation and aerosol–cloud interactions. *Clim. Dyn.* **53**: 3235–3256. DOI: 10.1007/s00382-019-04698-0.
 78. Cohen, J., Screen, J.A., Furtado, J.C., et al. (2014). Recent Arctic amplification and extreme mid-latitude weather. *Nat. Geosci.* **7**: 627–637. DOI: 10.1038/ngeo2234.
 79. Zhao, K., Wang, Y.J., Edwards, R.L., et al. (2020). Late Holocene monsoon precipitation changes in southern China and their linkage to Northern Hemisphere temperature. *Quat. Sci. Rev.* **232**: 106191. DOI: 10.1016/j.quascirev.2020.106191.
 80. Tan, L.C., Cai, Y.J., Cheng, H., et al. (2018). High-resolution monsoon precipitation changes on the southeastern Tibetan Plateau over the past 2300 years. *Quat. Sci. Rev.* **195**: 122–132. DOI: 10.1016/j.quascirev.2018.07.021.
 81. Tan, L.C., Cai, Y.J., An, Z.S., et al. (2016). Decreasing monsoon precipitation in southwest China during the last 240 years is associated with the warming of the tropical ocean. *Clim. Dyn.* **48**: 1769–1778.
 82. Frajka-Williams, E., Moat, B., Smeed, D., et al. (2021). Atlantic meridional overturning circulation observed by the RAPID-MOCHA-WBTS (RAPID-Meridional Overturning Circulation and Heatflux Array-Western Boundary Time Series) array at 26N from 2004 to 2020 (v2020. 1). British Oceanographic Data Centre-Natural Environment Research Council.

FUNDING AND ACKNOWLEDGMENTS

This study is supported by National Natural Science Foundation of China (NSFC 41888101, 42002199, 42150710534), Project (No. KDL&Guangxi202005) supported by Guangxi Key Science and Technology Innovation base on Karst Dynamics. We thank Prof. Liangcheng Tan for his important discussion for the mechanism and interpretation of oxygen isotope.

DECLARATION OF INTERESTS

Hai Cheng, Ashish Sinha, and Haiwei Zhang are Editorial Board members of The Innovation Geoscience and were blinded from reviewing or making final decisions on the manuscript. Peer review was handled independently of these members and their research group. The other authors declare no conflicts of interest.

DATA AND CODE AVAILABILITY

Data are available from the corresponding author upon reasonable request.

SUPPLEMENTAL INFORMATION

It can be found online at <https://doi.org/10.59717/j.xinn-geo.2023.100011>

LEAD CONTACT WEBSITE

<https://gr.xjtu.edu.cn/web/zjy1230/home>